Journal of Environmental Management 247 (2019) 766–775

Contents lists available at ScienceDirect

Journal of Environmental Management

journal homepage: www.elsevier.com/locate/jenvman

Research article

Exploring the impact of chemical composition on aerosol light extinction during winter in a heavily polluted urban area of China

Yaqing Zhou[a,b,c], Qiyuan Wang[a,b,c,d,*], Xu Zhang[e], Yichen Wang[f], Suixin Liu[a,b,d], Meng Wang[a,b,c], Jie Tian[a,b,d], Chongshu Zhu[a,b,d], Rujin Huang[a,b,d], Qian Zhang[g], Ting Zhang[a,b,d], Jiamao Zhou[a,b,d], Wenting Dai[a,b,d], Junji Cao[a,b,d,**]

[a] *State Key Laboratory of Loess and Quaternary Geology, Institute of Earth Environment, Chinese Academy of Sciences, Xi'an, 710061, China*
[b] *Key Laboratory of Aerosol Chemistry and Physics, Institute of Earth Environment, Chinese Academy of Sciences, Xi'an, 710061, China*
[c] *University of Chinese Academy of Sciences, Beijing, 100049, China*
[d] *CAS Center for Excellence in Quaternary Science and Global Change, Xi'an, 710061, China*
[e] *Xi'an Environmental Monitor Station, Xi'an, 710100, China*
[f] *College of Management, Shenzhen University, Shenzhen, 518060, China*
[g] *School of Environmental & Municipal Engineering, Xi'an University of Architecture and Technology, Xi'an, 710055, China*

ARTICLE INFO

Keywords:
PM_1
Aerosol species
Pollution formation mechanisms
Optical properties

ABSTRACT

An intensive measurement campaign was conducted in Xi'an, China from December 2012–January 2013 to investigate the chemical composition, formation, and optical properties of PM_1. The PM_1 mass concentration (average = 138.8 ± 83.2 $\mu g\,m^{-3}$) accounted for ~50% of the $PM_{2.5}$ mass. Organic aerosols (OA) and secondary inorganic aerosols (SIA) were the most abundant PM_1 components, contributing 53.0% and 35.0% to the mass, respectively. Both primary emissions and aqueous-phase oxidation of secondary aerosols played roles in the pollution episodes. The average light scattering and absorption coefficients during the campaign were 805 ± 581 Mm^{-1} and 123 ± 96 Mm^{-1}, respectively. Both the mass scattering and mass absorption efficiencies for PM_1 were higher than that for $PM_{2.5\text{-}1}$, indicating stronger ability of light extinction for the smaller particles at visible wavelengths compared with the larger ones. The contributions of aerosol species to light extinction coefficients under two visibility conditions were estimated based on multiple linear regression models, and the OA was found to be the largest contributor to light extinction in both cases. A larger contribution of SIA to light extinction for visibility < 5 km demonstrated its greater impacts on visibility during heavy pollution conditions. These findings provide insights into the importance of submicron particles for pollution and visibility degradation in northwestern China.

1. Introduction

Atmospheric aerosols affect the radiative and energy budgets of the atmosphere directly by scattering and absorbing solar radiation and indirectly by changing cloud reflectivity (Boucher, 2013; Wang et al., 2010). Aerosol optical properties, including the scattering coefficient (b_{scat}) and absorption coefficient (b_{abs}), are closely connected to the composition, size distributions, and morphological characteristics of the aerosol. Moreover, meteorological conditions, such as ambient relative humidity (RH), can affect hygroscopicity of the particle, which in turn affects the aerosol light extinction coefficient ($b_{ext} = b_{scat} + b_{abs}$) and ultimately visibility (Zieger et al., 2013). Atmospheric particulate matter (PM) mainly consists of organic matter (OM), secondary inorganic aerosols (SIA, including sulfate, nitrate, and ammonium), black carbon (BC), and soil dust. Of these, SIA and OM are the major light scattering components, which can exert cooling effects on the earth/atmosphere system, while the BC aerosol is strongly light absorbing and can cause global warming (Menon et al., 2002; Ramanathan and Carmichael, 2008). Recent studies also have shown that some types of OM, called brown carbon (BrC), also can absorb sunlight, especially in short wavelengths and as a result lead to radiative effects (Laskin et al., 2015).

---

[*] Corresponding author. State Key Laboratory of Loess and Quaternary Geology, Institute of Earth Environment, Chinese Academy of Sciences, Xi'an, 710061, China.

[**] Corresponding author. State Key Laboratory of Loess and Quaternary Geology, Institute of Earth Environment, Chinese Academy of Sciences, Xi'an, 710061, China.

E-mail addresses: wangqy@ieecas.cn (Q. Wang), cao@loess.llqg.ac.cn (J. Cao).

https://doi.org/10.1016/j.jenvman.2019.06.100
Received 5 November 2018; Received in revised form 4 May 2019; Accepted 23 June 2019
Available online 06 July 2019
0301-4797/ © 2019 Elsevier Ltd. All rights reserved.

The chemical components of PM are important determinants of the particles' optical properties, which also are affected by their size, shape, and mixing state (Seinfeld and Pandis, 2006). The relationship between the chemical components and b_{ext} has been investigated widely in China during last decade (e.g., Tao et al., 2014; Tian et al., 2015), but most of those studies relied on daily filter-based measurements, and thus, it was difficult to follow the optical properties of the aerosol during the evolution of pollution events. Many studies have used the Interagency Monitoring of Protected Visual Environments (IMPROVE) formula (Hand and Malm, 2007) to calculate the chemical b_{ext} (Cao et al., 2012; Tao et al., 2017; Zhou et al., 2017), but there is a shortcoming of this approach. That is, the mass extinction efficiencies for the chemical species used in the IMPROVE formula may not be the most appropriate for any specific region.

Recently, several campaigns have been conducted in China that involved high time-resolution measurements of chemical species and optical properties. For instance, Han et al. (2017) investigated differences in the contributions of chemical species to b_{ext} in Beijing during summer and winter, and they found that ammonium sulfate (30%) contributed the most to b_{ext} in summer while organic aerosol (OA) was the largest contributor (51%) in winter. Based on a positive matrix factor analysis of OA and the multiple linear regression method, Lan et al. (2018) found that secondary aerosols (79.4%) contributed more to light extinction than primary aerosols (20.6%) at Dongguan, in southeastern China. Results of a three months in Beijing, which involved real-time measurement of PM_1, showed a much higher contribution of secondary organic aerosol (SOA) to extinction compared with that from the primary organic aerosol (POA, Wang et al., 2015).

Although these studies have provided important information on physical and chemical properties of aerosols, the impacts of chemical species on aerosol optical properties relied on high time-resolution measurement are still not well constrained, especially in northwestern China where pollution is often serious (Li et al., 2016; Y. Wang et al., 2017b). Xi'an, the largest city in the northwestern China, has suffered from severe air pollution for decades as a result of the rapid urbanization, growth in motor vehicle usage, and large energy consumption in the region (H. Xu et al., 2016a). High mass concentrations of $PM_{2.5}$ (345–512 $\mu g\,m^{-3}$) have been reported throughout the year in Xi'an (Cao et al., 2012; Zhang et al., 2015), and the poor air quality and the potential effects on human health have led to increasing public concerns (http://xaepb.xa.gov.cn).

For this study, an intensive campaign was conducted at Xi'an during winter to measure aerosol chemical composition and aerosol light scattering and absorption at high time-resolution. The chemical evolution and optical characteristics of submicron particles under heavy pollution conditions were the main foci of the investigation. Further, the mass scattering and absorption efficiencies of primary and secondary organic aerosols, as well as SIA, were calculated using multiple linear regression models, and the contribution of each chemical component to the total b_{ext} was evaluated. The results of this study will help us understand the changes in aerosol populations and their optical properties under severe pollution conditions.

2. Experimental

2.1. Sampling site and instrumentation

Measurements were made in Xi'an, China from the rooftop of the Institute of Earth Environment, Chinese Academy of Sciences (34.23 °N, 108.88 °E, 10 m above ground level) from 23 December 2012 to 18 January 2013. The sampling site is situated within the high-tech region, which is southwest of the city center (Fig. S1), and it is encircled by office buildings and residential/commercial areas. Hourly $PM_{2.5}$ mass concentrations were measured with an E-BAM online sampler (Met One Instruments Inc., Washington, USA), which is an automatic air monitor that uses beta attenuation to estimate mass (Cheng et al., 2011).

The non-refractory submicron aerosol (NR-PM_1) was measured in situ using a quadrupole aerosol chemical speciation monitor (Q-ACSM, Aerodyne Research Inc., Billerica, Massachusetts), which operated at an air flow of 0.1 $L\,min^{-1}$ and had a time resolution of ~15 min (Detailed descriptions see Text S1). PM_1 mass was calculated as the sum of NR-PM_1 (including organics, SO_4^{2-}, NO_3^-, NH_4^+, and Cl^-) and BC, which was measured as described below. The mass concentrations of BC were measured with a single particle soot photometer (SP2) (Droplet Measurement Technology, Boulder, CO, USA), and detailed descriptions of this instrument can be found in Text S2 and elsewhere (e.g., Schwarz et al., 2006; G. Wang et al., 2018). A photoacoustic extinctiometer (PAX, Droplet Measurement Technology) was used to simultaneously measure the b_{scat} and b_{abs} at $\lambda = 532$ nm (Kok et al., 2010; Wei et al., 2013) (Detailed descriptions see Text S3). The calibration results for Q-ACSM, SP2 and PAX can be found in Fig. S2.

Hourly average nitrogen dioxide (NO_2), sulfur dioxide (SO_2), carbon monoxide (CO) and ozone (O_3) concentrations were measured by four online gaseous analyzers (EC9841 Nitrogen Oxides Analyzer, EC9850 Sulfur Dioxide Analyzer, EC9830 Carbon Monoxide Analyzer and EC9810 Ozone Analyzer, Ecotech, Melbourne, Australia, respectively). Hourly meteorological data, including relative humidity (RH), temperature, and wind speed, were measured with an automatic weather station (MAWS201, Vaisala, Vantaa, Finland) configured with a RH/temperature probe (Vaisala Model QMH101) and a wind sensor (Vaisala Model QMW101-M2). In addition, hourly boundary-layer heights were retrieved from the HYSPLIT Trajectory Model of NOAA, which was driven with the gridded meteorological data (Global Data Assimilation System, GDAS1, https://ready.arl.noaa.gov/HYSPLIT.php).

2.2. Data treatment and source analyses

Daily $PM_{2.5}$ filter samples were collected from 10:00 a.m. local time (LT, all time references below are given in LT) to 10:00 the next day with the use of a battery-powered mini-volume sampler (Airmetrics, Springfield, OR, USA). The filter-based $PM_{2.5}$ mass concentrations were used to correct the E-BAM mass data, and for this, the hourly $PM_{2.5}$ concentrations measured with the E-BAM were integrated over 24 h intervals (from 10:00 to 10:00 the next day) to match the filter-based $PM_{2.5}$ concentrations. As shown in Fig. S3, the average E-BAM $PM_{2.5}$ values exhibited a tight linear correlation with the gravimetric filter-based $PM_{2.5}$ mass loadings ($r = 0.98$). Based on this result, the hourly $PM_{2.5}$ mass concentrations measured with the E-BAM were adjusted by multiplying the mass by 1.34.

The organic aerosol was separated into two general components, that is, primary organic aerosol (POA) and oxygenated organic aerosol (OOA). These two OA components showed distinctly different mass spectral profiles, timeseries, and diurnal cycle characteristics. The mass concentration and composition of submicron particles measured with the Q-ACSM were analyzed using the standard ACSM data analysis software written in Igor Pro (WaveMetrics, Inc., Portland, OR., USA). The timeseries, diurnal cycles, mass spectra, and correlations with external tracers were analyzed using the Positive Matrix Factorization (PMF) technique and tested using the Igor Pro-based PMF Evaluation Tool (PET, v 2.04) (Ulbrich et al., 2009). The two components of OA, POA and OOA (see Fig. S4), were identified through these procedures.

As shown in Fig. S4, mass spectra with strong signals for $C_nH_{2n-1}^+$ (e.g., m/z 41, 55), $C_nH_{2n+1}^+$ (e.g., m/z 43, 57), and m/z 60 were defined as POA (Alfarra et al., 2007; Elser et al., 2016; Sun et al., 2016). The POA concentrations correlated well ($r = 0.80$–0.91) with those primary emission substances of CO, BC, and Cl^- (see Fig. S5), indicating that the reasonable identification of POA. The mass spectra of OOA were showed a prominent peak at m/z 44, which is consistent with patterns reported previously (Ng et al., 2010; Sun et al., 2016). Also, OOA showed a strong correlation with secondary inorganic species (including sulfate and nitrate) (Fig. S5).

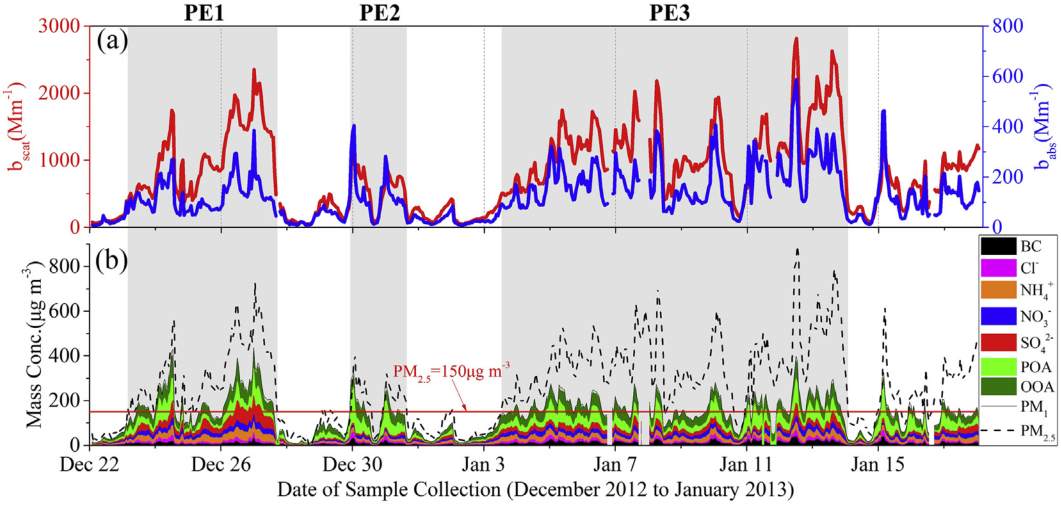

Fig. 1. Time series plots of (a) light scattering coefficient (b_{scat}) and absorption coefficient (b_{abs}); (b) mass concentrations of PM_1 and $PM_{2.5}$ and the main chemical species in PM_1 during the campaign. BC, POA, and OOA stand for black carbon, primary organic aerosol, and oxygenated organic aerosol. (For interpretation of the references to color in this figure legend, the reader is referred to the Web version of this article.)

3. Results and discussion

3.1. Aerosol mass concentration and chemical composition

The $PM_{2.5}$ mass concentrations varied from 3 to 894 μg m^{-3} over the course of the study (Fig. 1), and the arithmetic mean value (± standard deviation) was 264 ± 171 μg m^{-3}, which is 3.5 times higher than the China National Ambient Air Quality Grade II Standard (75 μg m^{-3}, GB3095-2012). Compared with previous studies conducted in Xi'an, the average $PM_{2.5}$ concentration was slightly higher than in the winters of 2006 (229.5 μg m^{-3}), 2008 (199.4 μg m^{-3}), and 2010 (233.0 μg m^{-3}) (H. Xu et al., 2016a). The PM_1 mass dominated the $PM_{2.5}$ mass concentration (see Fig. S6) and varied widely, from 7 to 436 μg m^{-3}, with an average of 138.8 ± 83.2 μg m^{-3}(Fig. 1). The mass concentrations of $PM_{2.5}$ and PM_1 were both larger than what has been reported for most wintertime studies in China, and they were several orders of magnitude higher than those typical cities of the U.S.A. or European countries (see Table S1). Therefore, the air quality in Xi'an during the study was extremely poor.

The average mass concentration of OA was 73.8 ± 46.8 μg m^{-3}; indeed, OA was the most abundant PM_1 species, and it accounted for 53.0% of PM_1 mass. The mass concentration of SIA was 48.6 μg m^{-3}, and it contributed more than 35.0% to the total PM_1 mass. The mass loading of BC (8.8 ± 7.2 μg m^{-3}) and Cl^- (7.6 ± 5.4 μg m^{-3}) were lower than OA and SIA, contributing 5.0% and 6.0% to PM_1 mass.

Fig. 2 shows the diurnal variations of PM_1 chemical species, and in it, the median values instead of averages were plotted to minimize the effects of extreme events. The median PM_1 mass concentration exhibited a pronounced diurnal cycle, with low values in the afternoon between 14:00 and 19:00 and high values from 21:00 to 01:00. This diurnal pattern can be explained by the variation of boundary-layer height, which was deep in the afternoon and shallow at night (Wang et al., 2016). As for PM_1 chemical species, the various groups of components showed distinct differences. For example, the mass concentrations of SO_4^{2-}, NO_3^-, and NH_4^+ showed similar diurnal patterns, which started to increase around 8:00 and reached a peak in the afternoon around 12:00–15:00. Although the deep boundary-layer height in the afternoon favored the dilution of the aerosol, the formation of SIA through heterogeneous reaction evidently offset the dilution effect (Sun et al., 2016). The observed diurnal pattern of ammonium generally followed the variations in the combined concentrations of SO_4^{2-}, NO_3^-, and Cl^- which represent for $(NH_4)_2SO_4$, NH_4NO_3, and NH_4Cl.

The OA showed a decreasing trend during the daytime but increased at night. As OA has multiple primary and secondary origins, an explanation for the diurnal cycle is complicated. As shown in Fig. 2, POA showed similar variation to the OA; that is, low mass loadings during the day and high loadings at night. The observed diurnal variability for POA is consistent with previous studies (Elser et al., 2016; Sun et al., 2013) that ascribed the variations to local emissions (e.g., traffic, biomass burning, and coal combustion) and changes in the boundary-layer height. In contrast to POA, OOA showed a peak from 10:00–14:00, which may be explained by photochemical production (Elser et al., 2016; Sun et al., 2014), and the ratio of OOA to OA showed a significant increase from 10:00–16:00 (Fig. S7). Chloride showed low concentrations in the afternoon and high concentrations in the early morning, suggesting that variations in the boundary-layer height and gas-aerosol partitioning (e.g., NH_4Cl partitioning) (Baek et al., 2006) affected its diurnal pattern. The BC mass concentration exhibited a diurnal pattern of “two peaks and two valleys”, which can be explained by the variations in boundary-layer height combined with the activity patterns of daily life (Wang et al., 2014).

3.2. Impacts of chemical species on pollution episodes

The causes for pollution are often complex due to the variety of aerosol processes (that is, photochemical and aqueous-phase production, removal, etc) and meteorological factors involved. To investigate the pollution formation in Xi'an, the $PM_{2.5}$ mass concentrations higher than 150 μg m^{-3} were classified as heavy pollution episodes (PE), whereas other days were referred to as the reference days (e.g., Liang et al., 2016; Sun et al., 2019). As shown in Fig. 1, three PEs occurred; these were PE1(24–28 December 2012), PE2 (30 December 2012–1 January 2013), and PE3 (4–14 January 2013). Fig. 3 shows the contributions of the chemical species to the PM_1 mass for each of the three PEs, and a statistical summary is presented in Table 1. The average mass concentrations of $PM_{2.5}$ were 332, 174, and 374 μg m^{-3} for PE1, PE2, and PE3, respectively, and these were 1.3–2.8 times larger than the average value for reference days (134 μg m^{-3}). The average mass concentrations of PM_1 were 201, 126, 175 μg m^{-3} during PE1, PE2, and PE3, respectively, and accounted for 62.3, 65.5, and 50.0% to the corresponding $PM_{2.5}$ mass. Moreover, the mass concentrations of PM_1 during the three PEs were 1.8–2.8 times larger than on the reference days.

For PE1, SIA and OA contributed similarly to the PM_1 mass, 45.4% and 44.8%, respectively (Fig. 3). To defined the difference in the

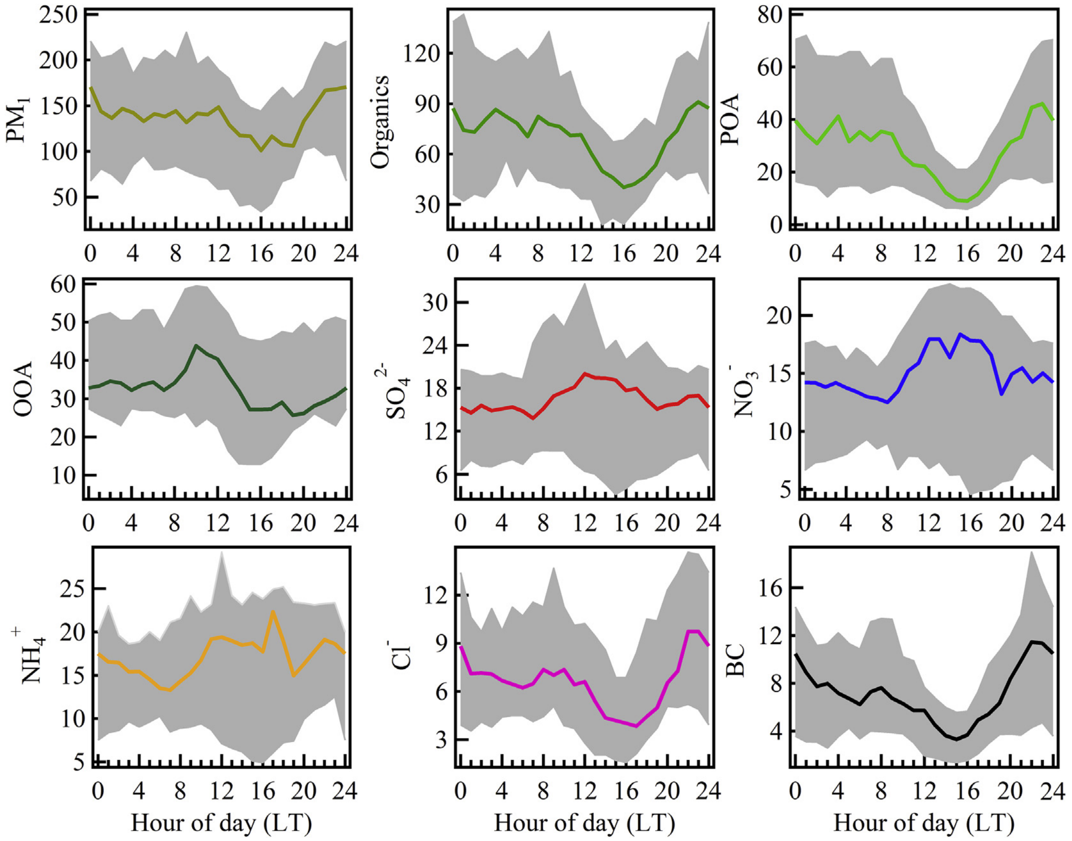

Fig. 2. Diurnal cycles of the mass concentrations (μg m^{-3}) of PM$_1$, organics, primary organic aerosol (POA), oxygenated organic aerosol (OOA), SO$_4^{2-}$, NO$_3^-$, NH$_4^+$, Cl$^-$, and black carbon (BC). The colored lines represent the median for each hour of the day, and the shaded areas show the range between the 10th and 90th percentiles of the data.

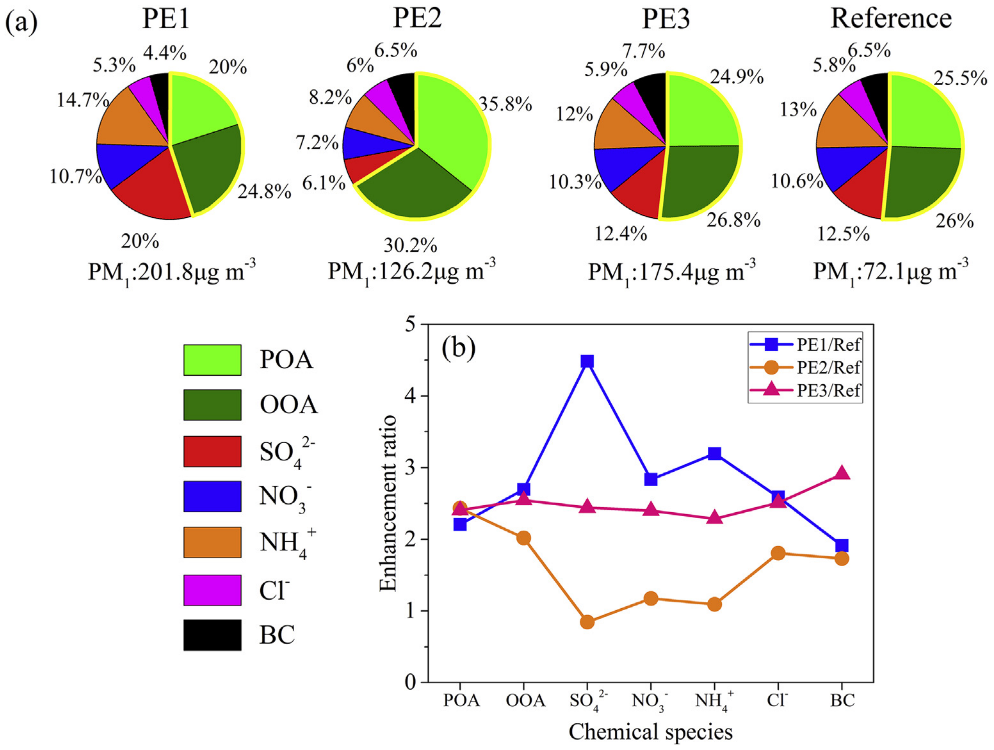

Fig. 3. (a) Arithmetic mean mass contribution of primary organic aerosol (POA), oxygenated organic aerosol (OOA), SO$_4^{2-}$, NO$_3^-$, NH$_4^+$, Cl$^-$, and black carbon (BC) to PM$_1$ mass during three pollution episodes and on reference days (areas outlined with thick yellow lines represent the organic aerosol); (b) Enhancement ratios of PM$_1$ chemical species concentrations between each pollution episode versus reference days. PE1, PE2, and PE3 represent pollution episodes that occurred from 24 to 28 December 2012, 30 December 2012–1 January 2013, and 4–14 January 2013, respectively. (For interpretation of the references to color in this figure legend, the reader is referred to the Web version of this article.)

Table 1

A summary of arithmetic mean $PM_{2.5}$ and PM_1 mass loadings, $PM_1/PM_{2.5}$ ratios, chemical species in PM_1, light scattering and absorption coefficients (b_{scat} and b_{abs}, respectively), meteorological conditions, ozone concentrations, and oxidation ratios during pollution episodes (PEs) and reference days.

Variable	PE1[a]	PE2	PE3	Reference days
Mass and chemical species loadings[b] ($\mu g\ m^{-3}$)				
$PM_{2.5}$	331.8 ± 142.9	173.8 ± 87.7	373.7 ± 148.9	134.2 ± 113.7
PM_1	201.8 ± 86.0	126.2 ± 73.5	175.4 ± 56.1	72.1 ± 58.0
$PM_1/PM_{2.5}$ ratio	0.62 ± 0.15	0.65 ± 0.14	0.50 ± 0.13	0.55 ± 0.20
POA	38.7 ± 27.4	42.7 ± 36.0	42.2 ± 22.9	17.5 ± 22.1
OOA	48.1 ± 18.1	36.0 ± 17.9	45.4 ± 11.4	17.8 ± 11.7
SO_4^{2-}	38.6 ± 21.2	7.3 ± 3.1	21.0 ± 7.7	8.6 ± 7.2
NO_3^-	20.7 ± 5.9	8.6 ± 3.5	17.5 ± 4.8	7.3 ± 5.7
NH_4^+	28.5 ± 9.9	9.8 ± 4.2	20.4 ± 6.0	8.9 ± 6.3
Cl^-	10.3 ± 5.1	7.2 ± 6.0	10.0 ± 4.7	4.0 ± 3.9
BC	8.6 ± 4.7	7.8 ± 6.5	13.1 ± 7.4	4.5 ± 5.3
Light extinction (Mm^{-1})				
b_{scat}	1075.1 ± 514.2	509.0 ± 278.0	1173.9 ± 524.9	357.9 ± 328.9
b_{abs}	127.0 ± 64.2	103.3 ± 80.6	183.0 ± 98.2	61.2 ± 65.4
Meteorological conditions[c]				
Visibility (km)	4.1 ± 2.1	10.2 ± 8.8	3.8 ± 2.7	20.5 ± 16.8
RH (%)	48.1 ± 12.1	29.3 ± 9.4	41.1 ± 10.4	32.6 ± 11.8
WS ($m\ s^{-1}$)	0.3 ± 0.2	0.2 ± 0.2	0.1 ± 0.1	0.5 ± 0.5
Boundary layer height (m)	200.7 ± 196.2	310.4 ± 291.2	207.8 ± 206.0	328.1 ± 305.4
Ozone (ppb) and oxidation ratios[d]				
O_3	3.6 ± 1.5	7.4 ± 7.7	4.3 ± 3.2	11.0 ± 8.2
SOR	0.11 ± 0.05	0.05 ± 0.01	0.06 ± 0.03	0.05 ± 0.02
NOR	0.33 ± 0.04	0.24 ± 0.07	0.30 ± 0.05	0.16 ± 0.07

[a] PE1, PE2, and PE3 represent pollution episodes on 24–28 December 2012, 30 December 2012–1 January 2013, and 4–14 January 2013, respectively.

[b] POA, OOA, and BC are primary organic aerosol, oxygenated organic aerosol, and black carbon, respectively.

[c] RH is relative humidity, and WS is wind speed.

[d] SOR and NOR denote molar ratios of SO_4^{2-} to SO_2 (SOR = $n\text{-}SO_4^{2-}/(n\text{-}SO_2+n\text{-}SO_4^{2-})$) and NO_3^- to NO_2 (NOR = $n\text{-}NO_3^-/(n\text{-}NO_2+n\text{-}NO_3^-)$), respectively.

concentration of chemical species during a pollution episode versus reference days, enhancement ratios were calculated as follows:

$$Enhancement\ ratio = [species]_{pollution}/[species]_{reference} \quad (1)$$

where [species] represents the concentration of the chemical species of interest, and the subscripts denote the pollution episodes and reference days. The enhancement ratios of all the measured chemical species were within range of 1.9–4.5 during PE1 compared with the reference days, and SO_4^{2-} increased the most.

To explore the mechanisms by which SIA formed, we calculated the molar ratios of SO_4^{2-} to SO_2 (Sulfur Oxidation Ratio, SOR = $n\text{-}SO_4^{2-}/(n\text{-}SO_2 + n\text{-}SO_4^{2-})$) and NO_3^- to NO_2 (Nitrogen Oxidation Ratio, NOR = $n\text{-}NO_3^-/(n\text{-}NO_2 + n\text{-}NO_3^-)$) to evaluate the sulfur and nitrogen partitioning between the particle and gas phases (Hu et al., 2014). For all data, temperature had only a weak relationship with SOR and NOR (Fig. 4a and c), suggesting a minor effect of temperature on SIA formation during the study. In contrast, SOR exhibited an obvious power function relationship with RH (Fig. 4b). That is, the SOR values were low and stable when the RH was less than 35.0%; however, as the RH increased to between 65.0% and 75.0%, the SOR increased rapidly. This indicates that sulfate formation was favored by high RH. Although the case was not as obvious for NOR, it also showed a positive correlation with RH (Fig. 4d). During this event, SOR, NOR, and RH were 0.11,0.33, and 48.1%, respectively, both SOR and NOR showed a clear increasing linear trend with RH, and the SOR during PE1 was twice than that on reference days (Fig. S8). Furthermore, as shown in Table 1, the concentration of ozone is lowest during PE1, and the visibility was considerably reduced, both of which indicate weak photochemical activity (Quan et al., 2014; Wang et al., 2001). Therefore, the enhancements of sulfate and nitrate during PE1 can be explained by the aqueous-phase oxidation of gas precursors such as SO_2 and NOx. The importance of aqueous-phase oxidation for the air pollution formation also has been recognized for some urban cities in north China (Q. Wang et al., 2018; Zhao et al., 2013).

The causes for PE2 evidently were unlike those for the two other PEs because chemical composition of the PM differed between the events. As shown in Fig. 3, OA accounted for a large majority (66.0%) of the PM_1 mass during PE2, and this was three times larger than the contribution from SIA (21.5%). Of the OA species, POA accounted for 35.8% of the PM_1 mass, which was larger than the contribution from OOA (30.2%). This indicates that the primary emissions of OA were important for the development of this second event. Moreover, it is noteworthy that the POA enhancement ratio was larger than that for OOA, indicating that organics from primary emissions were the main driving factors aggravating the extent of pollution for this event. The mass concentrations of SIA during PE2 were similar to those during reference days (Table 1), and this may be attributed to relatively weak aqueous-phase oxidation under low RH conditions (9.0–45.3%). The PE2 event lasted for only two days, and then the pollutants were dispersed by the light winds (> $1.0\ m\ s^{-1}$) on 1 January 2013.

During the last pollution episode (PE3), the concentrations of PM_1 and its major chemical components showed remarkable increases compared with the reference days. On 3 January, just before PE3, the RHs were low (16.4–26.7%), and the PM_1 mass concentrations varied from 11.0 to $41.2\ \mu g\ m^{-3}$. As the event developed, the PM_1 loadings increased gradually as the RH increased, presumably because that favored aqueous-phase oxidation led to high secondary aerosol loadings as discussed above. Meanwhile, low and steady wind speeds (average value of $0.1\ m\ s^{-1}$) and low boundary-layer heights (average value of 208 m) suppressed the dispersion of the pollutants, and that further aggravated the pollution event, which lasted for 10 days.

As shown in Fig. 3a, the PM_1 mass was dominated by OA (51.7%) during PE3, and the OA in turn, was composed of 48.2% of POA and a slightly higher amount of OOA (51.8%). However, when $PM_1 > 200\ \mu g\ m^{-3}$, the POA fraction of OA exceeded that from OOA (Fig. S9). This change in the POA fraction of OA highlights the importance of primary OA emissions for extremely polluted conditions. The contributions of SO_4^{2-}, NH_4^+, NO_3^-, BC, and Cl^- to PM_1 were 12.4, 12.0, 10.3, 7.7, and 5.9%, respectively. Compared with the reference days, the enhancement ratios for all chemical species during PE3 were comparable, ranging from 2.3 to 2.9.

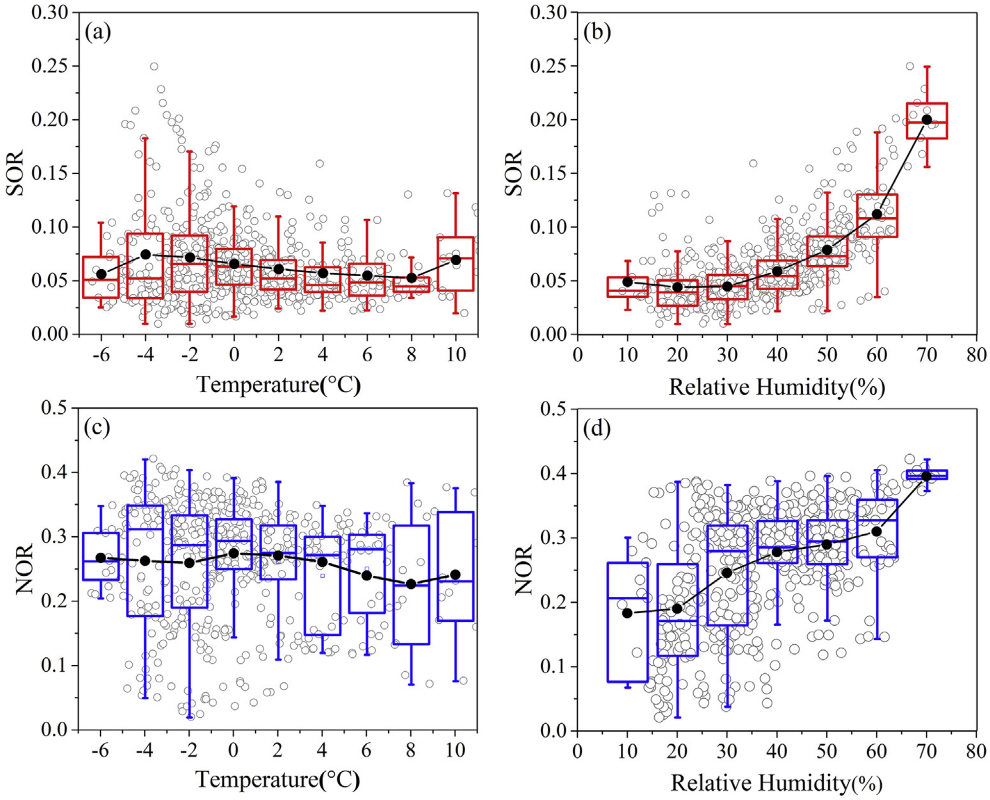

Fig. 4. Relationships between molar ratios of SO_4^{2-} to SO_2 versus (a) temperature and (b) relative humidity and the molar ratios of NO_3^- to NO_2 versus (c) temperature and (d) humidity. In each panel, the lower and upper edges of the boxes denote the 25% and 75% percentiles, respectively, while the vertical lines show the 10% and 90% percentiles.

3.3. Aerosol optical properties

3.3.1. Light extinction of PM_1 and $PM_{2.5}$

Aerosol light extinction exhibited dramatic day-to-day variations in Xi'an during the early to mid-winter study. As shown in Fig. 1a and 1b, the variations in b_{scat} tracked well with the $PM_{2.5}$ mass, and the hourly b_{scat} values ranged from 47 to 2815 Mm^{-1} during the campaign, with an average of 805 ± 581 Mm^{-1}. Although a relatively smaller magnitude than b_{scat} was found for b_{abs}, it also showed large variations from 7 to 587 Mm^{-1}, with an average value of 123 ± 96 Mm^{-1}.

Both b_{scat} and b_{abs} in the present study were higher than the values typically observed in and around China (see Table S2). The average b_{scat} was over three times higher than what has been reported for Beijing (256 Mm^{-1}, Zhou et al., 2017) and Lanzhou (240 Mm^{-1}, Pu et al., 2015) in China or Daejeon in Korea (189 Mm^{-1}, Jung et al., 2017), but it was lower than in Delhi, India (1027 Mm^{-1}, Tiwari et al., 2015). The average b_{abs} was a factor of 1.3–3.0 higher than at Beijing (43 Mm^{-1}, Zhou et al., 2017), Chengdu (60 Mm^{-1}, H. Wang et al., 2017a), and Guangzhou (96 Mm^{-1}, Tao et al., 2015b) in China, and it was is also higher than in surrounding countries such as India (86 Mm^{-1}, Tiwari et al., 2015) and Korea (21 Mm^{-1}, Jung et al., 2017).

As shown in Fig. 5a, b_{ext} exhibited a strong correlation with $PM_{2.5}$ mass ($r = 0.93$), and the specific $PM_{2.5}$ mass extinction efficiency was 3.6 $m^2 g^{-1}$. Although b_{ext} also exhibited a strong correlation ($r = 0.90$) with PM_1 mass, there were two clusters apparent in the data (Fig. 5b). The two groups were separated based on the average b_{ext} of 782 Mm^{-1}, which is equivalent to a visibility of 5.0 km based on the Koschmieder equation (Koschmieder, 1924). More important, the correlation of b_{ext} with PM_1 mass was stronger when visibility was > 5.0 km ($r = 0.96$) than when visibility was < 5.0 km ($r = 0.73$) (see in Fig. S10). This result can be attributed to a larger proportion of $PM_{2.5\text{-}1}$ (the difference between $PM_{2.5}$ and PM_1 masses) relative to PM_1 when the visibility was lower.

Previous studies have indicated that PM_1 often has a large impact on visibility (Hyslop, 2009; Watson, 2002), and the highest mass extinction efficiency of PM lies in the particle size range of 0.1–1.0 μm (Huang et al., 2013; Seinfeld and Pandis, 2006). In this study, the mass scattering efficiency (MSE) and mass absorption efficiency (MAE) of PM_1 and $PM_{2.5\text{-}1}$ were estimated using linear regression and the following formulas based on MSE (or MAE) theory (Hand and Malm, 2007; Titos et al., 2012):

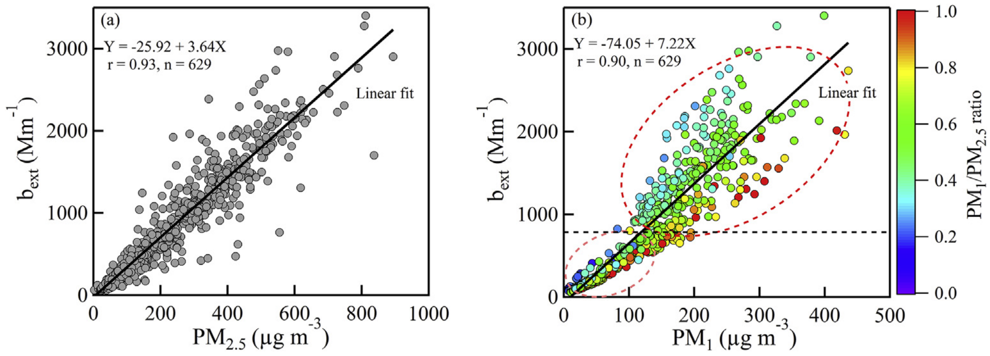

Fig. 5. Scatter plots of light extinction coefficients (b_{ext}) versus mass concentrations of (a) $PM_{2.5}$ and (b) PM_1. Data points are color-coded based on $PM_1/PM_{2.5}$ ratios. The horizontal dashed black line represents the b_{ext} of 782 Mm^{-1} (equivalent to visibility = 5.0 km). The red dashed ovals represent the two clusters with visibility greater or less than 5.0 km. (For interpretation of the references to color in this figure legend, the reader is referred to the Web version of this article.)

Table 2

Summary statistics for mass scattering and mass absorption efficiencies (units: $m^2\ g^{-1}$) for selected PM_1 chemical species under different visibility conditions.

	Mass scattering efficiency				Mass absorption efficiency		
	POA[a]	OOA	$(NH_4)_2SO_4$	NH_4NO_3	BC	OOA	POA
Visibility > 5 km (HV)	4.1	3.9	3.6	8.9	9.7	0.47	0.20
Visibility < 5 km (LV)	6.1	2.7	6.0	17.4	13.2	0.68	−0.33

[a] POA, OOA, and BC stand for primary organic aerosol, oxygenated organic aerosol, and black carbon, respectively.

$$b_{scat} = MSE_{PM_1} \times [PM_1] + MSE_{PM_{2.5-1}} \times [PM_{2.5-1}] \tag{2}$$

$$b_{abs} = MAE_{PM_1} \times [PM_1] + MAE_{PM_{2.5-1}} \times [PM_{2.5-1}] \tag{3}$$

where MSE_{PM_1} and $MSE_{PM_{2.5-1}}$ are the MSEs for PM_1 and $PM_{2.5\text{-}1}$, respectively; MAE_{PM_1} and $MAE_{PM_{2.5-1}}$ are the MAEs for PM_1 and $PM_{2.5\text{-}1}$; and $[PM_1]$ and $[PM_{2.5\text{-}1}]$ represent the mass concentrations of PM_1 and $PM_{2.5\text{-}1}$. About 70% of the measured data were randomly selected for use in these calculations, while the other 30% of the data were used to verify the validity and accuracy of the method. As shown in Fig. S11, the estimated versus measured b_{scat} and b_{abs} values were strongly correlated (b_{scat} slope = 0.94, r = 0.99 and b_{abs} slope = 0.90, r = 0.96), and this demonstrates the validity of the approach.

The calculated MSE for PM_1 was 4.1 ± 0.1 $m^2\ g^{-1}$, which is consistent with theoretical values (3.7–4.1 $m^2\ g^{-1}$) calculated using Mie theory (Bates et al., 2005; Boucher and Anderson, 1995; Garland et al., 2008), and it also was comparable with the values observed at Beijing (3.6 $m^2\ g^{-1}$, X. Xu et al., 2016b) and Guangzhou (4.3 $m^2\ g^{-1}$, Xia et al., 2017), China during winter. The MSE for $PM_{2.5\text{-}1}$ was 2.1 ± 0.1 $m^2\ g^{-1}$, and that was smaller than the PM_1 MSE. Furthermore, the estimated MAE for PM_1 was 0.76 ± 0.03 $m^2\ g^{-1}$, which was five-fold higher than that for $PM_{2.5\text{-}1}$ (0.15 ± 0.03 $m^2\ g^{-1}$). The MAE for PM_1 in this study was close to the value found during winter in Beijing (0.7 $m^2\ g^{-1}$, X. Xu et al., 2016b). The larger MSE and MAE values for PM_1 relative to $PM_{2.5\text{-}1}$ indicate stronger ability of light extinction for the small particles (diameters < 1 μm) than larger ones at visible wavelengths. Results based on Equations (2) and (3), showing that PM_1 accounted for 71.9% of b_{scat} and 85.7% of b_{abs} when visibility was > 5 km, and that the contributions of PM_1 to b_{scat} and b_{abs} decreased to 67.0% and 83.5% when visibility was < 5 km.

3.3.2. Impacts of chemical species on aerosol light extinction

To explore possible connections between chemical species and aerosol light extinction, we divided the data into two groups to investigate relationships between b_{ext} and PM_1 (see Fig. 5b as discussed in Section 3.3.1). The first group was for data when visibility > 5 km (HV) and the second for low visibility < 5 km (LV). The 5 km visibility threshold has been used in several earlier studies to identify heavy pollution episodes (e.g., Cao et al., 2012; Fu et al., 2013; Li et al., 2016). Previous studies have shown that b_{ext} can be reconstructed from the mass concentrations of aerosol chemical species and the corresponding MSEs and MAEs (Hand and Malm, 2007; Titos et al., 2012), and this is the approach we used for our analysis.

Of the various aerosol chemical constituents, $(NH_4)_2SO_4$, NH_4HSO_4, NH_4NO_3, and OA (including POA and OOA) are normally the main particulate scatterers of sunlight in the atmosphere (Cao et al., 2012; Zhou et al., 2017). During our campaign, there was sufficient NH_4^+ to neutralize the SO_4^{2-} and NO_3^- (see Fig. S12), and therefore, the mass concentrations of $(NH_4)_2SO_4$ and NH_4NO_3 were calculated from the molar ratios of $(NH_4)_2SO_4$ to SO_4^{2-} and NH_4NO_3 to NO_3^-. That is, $(NH_4)_2SO_4 = 1.375 \times [SO_4^{2-}]$ and $NH_4NO_3 = 1.29 \times [NO_3^-]$ (Tao et al., 2015a).

The two light-absorbing carbonaceous aerosol species are BC and BrC (Andreae and Gelencsér, 2006; Yang et al., 2009). Of these, BC forms through the incomplete combustion process whereas BrC has multiple sources, including primary emissions and secondary formation; thus, both POA and OOA have light-absorbing properties.

Two of the key aerosol optical properties, b_{scat} and b_{abs}, can be calculated from the following equations:

$$b_{scat} = MSE((NH_4)_2SO_4) \times [(NH_4)_2SO_4] + MSE(NH_4NO_3) \times [NH_4NO_3] + MSE(POA) \times [POA] + MSE(OOA) \times [OOA] + a \tag{4}$$

$$b_{abs} = MAE(BC) \times [BC] + MAE(POA) \times [POA] + MAE(OOA) \times [OOA] + b \tag{5}$$

where the chemical substance enclosed in parentheses is used to show the MSE or MAE for each scattering or absorbing species in PM_1; the brackets denote the mass concentrations of individual species; a and b represent other light scattering and absorbing species, respectively. The mass concentration of a chemical substance was multiplied by the corresponding MSE (or MAE) to obtain the light scattering (or absorption) coefficient for the species. In the absence of detailed information on the microphysical and chemical structure of the aerosols, the calculations were based on the assumption of external mixed among the chemical species. We note that the aerosol optical properties can be affected by the particles' mixing state, but it has been shown that light extinction is not particularly sensitive to external or internal mixing of the aerosol (Malm and Kreidenweis, 1997; Sloane, 1986).

The reconstructed b_{scat} (r = 0.95 for HV and 0.72 for LV) and b_{abs} (r = 0.99 for both HV and LV conditions) showed strong correlations with the measured values (Fig. S13), indicating that the multiple linear regression models accurately reconstructed the b_{scat} and b_{abs} for PM_1 from the chemical composition data. Furthermore, the slope of the reconstructed b_{scat} versus the measured b_{scat} was close to 1.0 (slope = 0.91) for the HV group, but it was considerably smaller (0.51) for the LV group. This may be due to a greater contribution from the $PM_{2.5\text{-}1}$ to b_{scat} for the more heavily polluted condition.

The MSEs for POA, $(NH_4)_2SO_4$, and NH_4NO_3 in PM_1 were 1.5–2.0 times higher for the LV condition compared with the HV group (Table 2). The MSE for $(NH_4)_2SO_4$ in the LV condition was within the range of 5.2–7.0 $m^2\ g^{-1}$ observed in Beijing (Han et al., 2015; Wang et al., 2015), whereas the $(NH_4)_2SO_4$ MSE for HV condition was smaller. The NH_4NO_3 MSEs for both types of visibility conditions were larger than those found in Beijing (6.0–7.0 $m^2\ g^{-1}$, Han et al., 2015; Wang et al., 2015). For POA and OOA, the calculated MSEs were comparable to values reported in previous studies (1.0–16.7 $m^2\ g^{-1}$, Han et al., 2015; Lan et al., 2018; Wang et al., 2015). The MAEs for BC and OOA varied widely, but higher values for both of these species were found for the lower visibility condition. The BC MAEs for both HV and LV conditions (9.7 and 13.2 $m^2\ g^{-1}$, respectively) were comparable with those found in Beijing on clean days (7–14 $m^2\ g^{-1}$, with average of 10.3 $m^2\ g^{-1}$; X. Xu et al., 2016b) and Nanjing (10.5–11.4 $m^2\ g^{-1}$ throughout the year; Tao et al., 2018), but they were much lower than what has been reported for polluted conditions in some other cities where the MAEs for BC ranged from 10 to 50 $m^2\ g^{-1}$ (Chan et al., 2011; X. Xu et al., 2016b).

The OA accounted for the largest fraction of b_{ext} for both the HV and LV conditions, 43.8 and 31.3%, respectively (Fig. 6). Further, the contribution of OOA to b_{ext} was larger than POA under the HV condition (18.5 for POA and 25.3% for OOA), whereas the contribution of POA (20.2%) exceeded that of OOA (11.1%) under LV condition—this

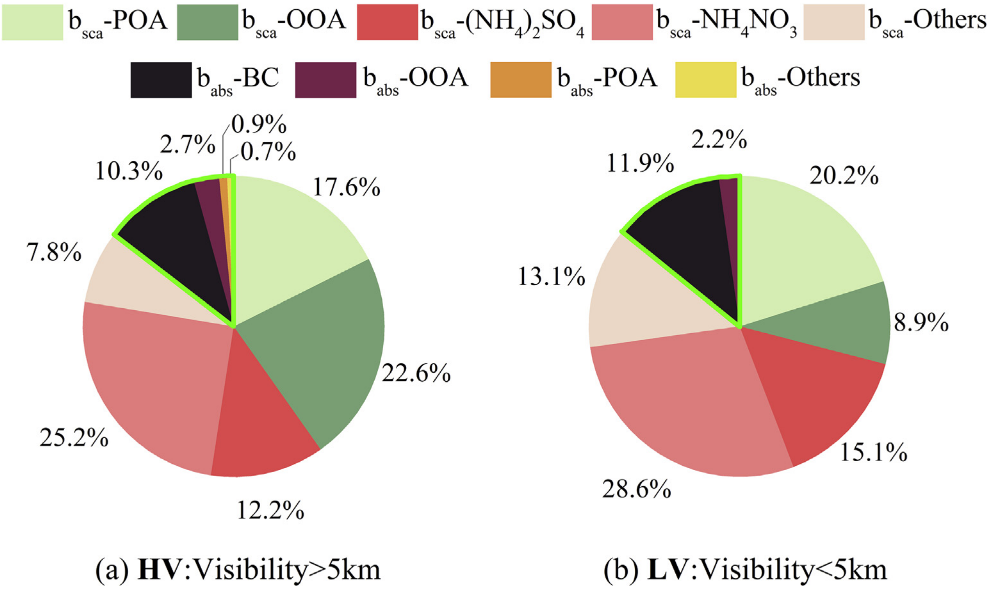

(a) **HV**:Visibility>5km　(b) **LV**:Visibility<5km

Fig. 6. Contributions of primary organic aerosol (POA), oxygenated organic aerosol (OOA), $(NH_4)_2SO_4$, NH_4NO_3, black carbon (BC), and other materials (others) to light extinction coefficients under different visibility conditions (Area outlined in green represents the absorption coefficient). b_{scat} and b_{abs} represent the light scattering and absorption coefficients, respectively. (For interpretation of the references to color in this figure legend, the reader is referred to the Web version of this article.)

can be explained by the large mass fraction of POA during the pollution events. The second largest contributor to b_{ext} was NH_4NO_3, which accounted for 25.2% and 28.6% of the values during the HV and LV conditions, respectively. This indicates that NH_4NO_3 played an important role in reducing visibility, and that is consistent with the growing impact of nitrate on haze formation over China caused by a continuous increase in NOx emissions during last decades (Wang et al., 2013). For $(NH_4)_2SO_4$, the contributions to b_{ext} were 12.2% for the HV and 15.1% for the LV condition. Interestingly, the combined contribution of NH_4NO_3 and $(NH_4)_2SO_4$ (43.7%) to b_{ext} under LV condition exceeded that of OA (31.3%), which indicates that secondary inorganic species played critical role in visibility degradation during heavy pollution condition. The fraction of the absorption coefficient attributed to BC and OOA (10–12% and 2–3%, respectively) showed no significant change between the LV and HV conditions.

4. Conclusions

High time-resolution measurements of aerosol light extinction and PM_1 composition at an urban site in Xi'an, China were made from 23 December 2012 to 18 January 2013. Changes in PM_1 chemical composition were investigated for three pollution episodes, and MSE and MAE for each PM_1 chemical components were calculated to determine the impacts of specific chemical species on aerosol light extinction. The mass concentrations of $PM_{2.5}$ varied dramatically and averaged $264 \pm 171\,\mu g\,m^{-3}$ while the average PM_1 mass concentration was $138.8 \pm 83.2\,\mu g\,m^{-3}$, thus accounting for ~50.0% of the $PM_{2.5}$ mass. Both the $PM_{2.5}$ and PM_1 loadings in this study were higher than the reported values for most cities in China, indicating that severe air pollution in Xi'an during winter.

During three pollution episodes, the PM_1 mass loadings were 1.8–2.8 times larger than during the reference days. The PE1 was characterized by a strong contribution of SIA (45.4%) to the PM_1 mass, and that was likely caused by the aqueous-phase oxidation of gas precursors. Unlike the two other PEs, OA contributed the largest percentage (66.0%) of the PM_1 mass during PE2, and the emission of POA was important during the evolution of that pollution episode. The chemical composition of the aerosol during PE3 was similar to that on the reference days, but the concentration were ~2-fold higher due to meteorological conditions unfavorable for the dispersal of pollutants.

The average b_{scat} and b_{abs} values were $805 \pm 581\,Mm^{-1}$ and $123 \pm 96\,Mm^{-1}$, respectively. The MSE and MAE values for PM_1, which were calculated using a multiple linear regression model, were higher than those for $PM_{2.5\text{-}1}$ indicating that small particles played stronger ability of light extinction. The MSEs for POA, ammonium sulfate, and ammonium nitrate were 1.5–2.0 times greater for low visibility conditions compared with high visibility days. The OA accounted for the largest fraction of b_{ext} (43.8% for the HV and 31.3% for LV condition), while the contribution of POA (20.2%) exceeded that of OOA (11.1%) for the LV condition. Overall, NH_4NO_3 was second largest contributor to b_{ext}, accounting for 25.2% of the effect when the visibility was > 5 km and 28.6% when the visibility was less than that. BC also accounted for a considerable and relatively stable proportion of the b_{ext} (10.3% for the HV and 11.9% for LV condition). A chemical extinction apportionment showed that secondary inorganic aerosols played an especially important role in visibility degradation when the air pollution was severe.

Competing interests

The authors declare that they have no competing financial interest in relation to this study.

Acknowledgments

This research was supported by the National Natural Science Foundation of China (21661132005), the Key Research and Development Program of Shaanxi Province (2018ZDCXL-SF-30-5), and the National Key Research and Development Program granted by Ministry of Science & Technology of China (No. 2017YFC0212200). Qiyuan Wang acknowledges support from the Youth Innovation Promotion Association, Chinese Academy of Sciences (2019402).

Appendix A. Supplementary data

Supplementary data to this article can be found online at https://doi.org/10.1016/j.jenvman.2019.06.100.

References

Alfarra, M.R., Prévôt, A.S.H., Szidat, S., Sandradewi, J., Weimer, S., Lanz, V.A., Schreiber, D., Mohr, M., Baltensperger, U., 2007. Identification of the mass spectral signature of organic aerosols from wood burning emissions. Environ. Sci. Technol. 41, 5770–5777.
Andreae, M.O., Gelencsér, A., 2006. Black carbon or brown carbon? The nature of light-absorbing carbonaceous aerosols. Atmos. Chem. Phys. 6, 3131–3148.
Baek, B.H., Koziel, J., Aneja, V.P., 2006. A preliminary review of gas-to-particle

conversion, monitoring, and modeling efforts in the USA. Int. J. Glob Environ. Issues 6, 204–230.

Bates, T.S., Quinn, P.K., Coffman, D.J., Johnson, J.E., Middlebrook, A.M., 2005. Dominance of organic aerosols in the marine boundary layer over the gulf of Maine during NEAQS 2002 and their role in aerosol light scattering. J. Geophys. Res. Atmos. 110, D18202.

Boucher, O., Anderson, T.L., 1995. General circulation model assessment of the sensitivity of direct climate forcing by anthropogenic sulfate aerosols to aerosol size and chemistry. J. Geophys. Res. Atmos. 100, 26117–26134.

Boucher, O., 2013. Clouds and aerosols. In: Climate Change 2013: the Physical Science Basis. Contribution of Working Group I to the Fifth Assessment Report of the Intergovernmental Panel on Climate Change. Cambridge Univ. Press, Cambridge, U. K., and New York, pp. 876–927.

Cao, J.J., Wang, Q.Y., Chow, J.C., Watson, J.G., Tie, X.X., Shen, Z.X., Wang, P., An, Z.S., 2012. Impacts of aerosol compositions on visibility impairment in Xi'an, China. Atmos. Environ. Times 59, 559–566.

Chan, T.W., Brook, J.R., Smallwood, G.J., Lu, G., 2011. Time resolved measurements of black carbon light absorption enhancement in urban and near-urban locations of southern Ontario, Canada. Atmos. Chem. Phys. 11, 10407–10432.

Cheng, Y.H., Chang, H.P., Hsieh, C.J., 2011. Short-term exposure to PM_{10}, $PM_{2.5}$, ultrafine particles and CO_2 for passengers at an intercity bus terminal. Atmos. Environ. 45, 2034–2042.

Elser, M., Huang, R.-J., Wolf, R., Slowik, J.G., Wang, Q., Canonaco, F., Li, G., Bozzetti, C., Daellenbach, K.R., Huang, Y., Zhang, R., Li, Z., Cao, J., Baltensperger, U., El-Haddad, I., Prévôt, A.S.H., 2016. New insights into $PM_{2.5}$ chemical composition and sources in two major cities in China during extreme haze events using aerosol mass spectrometry. Atmos. Chem. Phys. 16, 3207–3225.

Fu, C., Wu, J., Gao, Y., Zhao, D., Han, Z., 2013. Consecutive extreme visibility events in China during 1960-2009. Atmos. Environ. 68, 1–7.

Garland, R.M., Yang, H., Schmid, O., Rose, D., Nowak, A., Achtert, P., Wiedensohler, A., Takegawa, N., Kita, K., Miyazaki, Y., Kondo, Y., Hu, M., Shao, M., Zeng, L.M., Zhang, Y.H., Andreae, M.O., Pöschl, U., 2008. Aerosol optical properties in a rural environment near the mega-city Guangzhou, China: implications for regional air pollution, radiative forcing and remote sensing. Atmos. Chem. Phys. 8, 5161–5186.

Han, T.T., Xu, W.Q., Chen, C., Liu, X.G., Wang, Q.Q., Li, J., Zhao, X.J., Du, W., Wang, Z.F., Sun, Y.L., 2015. Chemical apportionment of aerosol optical properties during the Asia-Pacific Economic Cooperation summit in Beijing, China. J. Geophys. Res. Atmos. 120, 12281–12295.

Han, T.T., Xu, W.Q., Li, J., Freedman, A., Zhao, J., Wang, Q.Q., Chen, C., Zhang, Y.J., Wang, Z.F., Fu, P.Q., Liu, X.G., Sun, Y.L., 2017. Aerosol optical properties measurements by a CAPS single scattering albedo monitor: comparisons between summer and winter in Beijing, China. J. Geophys. Res. Atmos. 122, 2513–2526.

Hand, J.L., Malm, W.C., 2007. Review of aerosol mass scattering efficiencies from ground-based measurements since 1990. J. Geophys. Res. Atmos. 112, 321–341.

Hu, G.Y., Zhang, Y.M., Sun, J.Y., Zhang, L.M., Shen, X.J., Lin, W.L., Yang, Y., 2014. Variability, formation and acidity of water-soluble ions in $PM_{2.5}$ in Beijing based on the semi-continuous observations. Atmos. Res. 145, 1–11.

Huang, Y., Li, L., Li, J., Wang, X., Chen, H., Chen, J., Yang, X., Gross, D.S., Wang, H., Qiao, L., Chen, C., 2013. A case study of the highly time-resolved evolution of aerosol chemical and optical properties in urban Shanghai, China. Atmos. Chem. Phys. 13, 3931–3944.

Hyslop, N.P., 2009. Impaired visibility: the air pollution people see. Atmos. Environ. 43, 182–195.

Jung, J., Yu, J., Lyu, Y., Lee, M., Hwang, T., Lee, S., 2017. Ground-based characterization of aerosol spectral optical properties of haze and Asian dust episodes under Asian continental outflow during winter 2014. Atmos. Chem. Phys. 17, 5297–5309.

Kok, G., Walker, J.W., Arnott, W.P., Arnold, I.J., Keady, P.B., 2010. Photoacoustic extinctiometer (PAX): a new instrument for measurement of climate-relevant optical properties of aerosols. In: AAAR 29th Annual Conference. Oregon Convention Center, Portland, Oregon, USA.

Koschmieder, H., 1924. Theorie der horizontalen Sichtweite. Beitrage zur Physik der freien Atmosphare, pp. 33–53.

Lan, Z.J., Zhang, B., Huang, X.F., Zhu, Q., Yuan, J.F., Zeng, L.W., Hu, M., He, L.Y., 2018. Source apportionment of $PM_{2.5}$ light extinction in an urban atmosphere in China. J. Environ. Sci. China. 63, 277–284.

Laskin, A., Laskin, J., Nizkorodov, S.A., 2015. Chemistry of atmospheric brown carbon. Chem. Rev. 115, 4335–4382.

Li, J., Wang, G., Ren, Y., Wang, J., Wu, C., Han, Y., Zhang, L., Cheng, C., Meng, J., 2016. Identification of chemical compositions and sources of atmospheric aerosols in Xi'an, inland China during two types of haze events. Sci. Total Environ. 566, 230–237.

Liang, X., Li, S., Zhang, S., Huang, H., Chen, S.X., 2016. $PM_{2.5}$ data reliability, consistency, and air quality assessment in five Chinese cities. J. Geophys. Res. Atmos. 121, 10220–10236.

Malm, W.C., Kreidenweis, S.M., 1997. The effects of models of aerosol hygroscopicity on the apportionment of extinction. Atmos. Environ. 31, 1965–1976.

Menon, S., Hansen, J., Nazarenko, L., Luo, Y.F., 2002. Climate effects of black carbon aerosols in China and India. Science 297, 2250–2253.

Ng, N.L., Canagaratna, M.R., Zhang, Q., Jimenez, J.L., Tian, J., Ulbrich, I.M., Kroll, J.H., Docherty, K.S., Chhabra, P.S., Bahreini, R., Murphy, S.M., Seinfeld, J.H., Hildebrandt, L., Donahue, N.M., DeCarlo, P.F., Lanz, V.A., Prévôt, A.S.H., Dinar, E., Rudich, Y., Worsnop, D.R., 2010. Organic aerosol components observed in northern hemispheric datasets from aerosol mass spectrometry. Atmos. Chem. Phys. 10, 4625–4641.

Pu, W., Wang, X., Zhang, X., Ren, Y., Shi, J.-S., Bi, J.-R., Zhang, B.-D., 2015. Size distribution and optical properties of particulate matter (PM_{10}) and black carbon (BC) during dust storms and local air pollution events across a loess plateau site. Aerosol. Air. Qual. Res. 15, 2212–2224.

Quan, J., Tie, X., Zhang, Q., Liu, Q., Li, X., Gao, Y., Zhao, D., 2014. Characteristics of heavy aerosol pollution during the 2012–2013 winter in Beijing, China. Atmos. Environ. Times 88, 83–89.

Ramanathan, V., Carmichael, G., 2008. Global and regional climate changes due to black carbon. Nat. Geosci. 1, 221–227.

Schwarz, J.P., Gao, R.S., Fahey, D.W., Thomson, D.S., Watts, L.A., Wilson, J.C., Reeves, J.M., Darbeheshti, M., Baumgardner, D.G., Kok, G.L., Chung, S.H., Schulz, M., Hendricks, J., Lauer, A., Karcher, B., Slowik, J.G., Rosenlof, K.H., Thompson, T.L., Langford, A.O., Loewenstein, M., Aikin, K.C., 2006. Single-particle measurements of midlatitude black carbon and light-scattering aerosols from the boundary layer to the lower stratosphere. J. Geophys. Res. Atmos. 111, D16207.

Seinfeld, J.H., Pandis, S.N., 2006. Atmospheric Chemistry and Physics: from Air Pollution to Climate Change, second ed. John Wiley & Sons, New York.

Sloane, C.S., 1986. Effect of composition on aerosol light scattering efficiencies. Atmos. Environ. 20, 1025–1037.

Sun, J., Liang, M., Shi, Z., Shen, F., Li, J., Huang, L., Ge, X., Chen, Q., Sun, Y., Zhang, Y., Chang, Y., Ji, D., Ying, Q., Zhang, H., Kota, H., Hu, J., 2019. Investigating the $PM_{2.5}$ mass concentration growth processes during 2013-2016 in Beijing and Shanghai. Chemosphere 221, 452–463.

Sun, Y.L., Wang, Z.F., Fu, P.Q., Yang, T., Jiang, Q., Dong, H.B., Li, J., Jia, J.J., 2013. Aerosol composition, sources and processes during wintertime in Beijing, China. Atmos. Chem. Phys. 13, 4577–4592.

Sun, Y.L., Jiang, Q., Wang, Z., Fu, P., Li, J., Yang, T., Yin, Y., 2014. Investigation of the sources and evolution processes of severe haze pollution in Beijing in January 2013. J. Geophys. Res. Atmos. 119, 4380–4398.

Sun, Y.L., Du, W., Fu, P., Wang, Q., Li, J., Ge, X., Zhang, Q., Zhu, C., Ren, L., Xu, W., Zhao, J., Han, T., Worsnop, D.R., Wang, Z., 2016. Primary and secondary aerosols in Beijing in winter: sources, variations and processes. Atmos. Chem. Phys. 16, 8309–8329.

Tao, J., Zhang, L., Cao, J., Hsu, S.C., Xia, X., Zhang, Z., Lin, Z., Cheng, T., Zhang, R., 2014. Characterization and source apportionment of aerosol light extinction in Chengdu, southwest China. Atmos. Environ. 95, 552–562.

Tao, J., Zhang, L., Gao, J., Wang, H., Chai, F., Wang, S., 2015a. Aerosol chemical composition and light scattering during a winter season in Beijing. Atmos. Environ. 110, 36–44.

Tao, J., Zhang, L., Zhang, Z., Huang, R., Wu, Y., Zhang, R., Cao, J., Zhang, Y., 2015b. Control of $PM_{2.5}$ in Guangzhou during the 16th Asian games period: implication for hazy weather prevention. Sci. Total Environ. 508, 57–66.

Tao, J., Zhang, L., Cao, J., Zhang, R., 2017. A review of current knowledge concerning $PM_{2.5}$ chemical composition, aerosol optical properties and their relationships across China. Atmos. Chem. Phys. 17, 9485–9518.

Tao, J., Zhang, Z., Wu, Y., Lin, Z., Cao, J., Shen, Z., Zhang, R., 2018. Characteristics of mass absorption efficiency of elemental carbon in urban Chengdu, southwest China: implication for the coating effects on aerosol absorption. Aerosol. Sci. Eng. 2, 33–41.

Tian, P., Wang, G., Zhang, R., Wu, Y., Yan, P., 2015. Impacts of aerosol chemical compositions on optical properties in urban Beijing, China. Particuology 18, 155–164.

Titos, G., Foyo-Moreno, I., Lyamani, H., Querol, X., Alastuey, A., Alados-Arboledas, L., 2012. Optical properties and chemical composition of aerosol particles at an urban location: an estimation of the aerosol mass scattering and absorption efficiencies. J. Geophys. Res. Atmos. 117, D4.

Tiwari, S., Pandithurai, G., Attri, S.D., Srivastava, A.K., Soni, V.K., Bisht, D.S., Kumar, V.A., Srivastava, M.K., 2015. Aerosol optical properties and their relationship with meteorological parameters during wintertime in Delhi, India. Atmos. Res. 153, 465–479.

Ulbrich, I.M., Canagaratna, M.R., Zhang, Q., Worsnop, D.R., Jimenez, J.L., 2009. Interpretation of organic components from Positive Matrix Factorization of aerosol mass spectrometric data. Atmos. Chem. Phys. 9, 2891–2918.

Wang, G., Zhang, F., Peng, J., Duan, L., Ji, Y., Marrero-Ortiz, W., Wang, J., Li, J., Wu, C., Cao, C., Wang, Y., Zheng, J., Secrest, J., Li, Y., Wang, Y., Li, H., Li, N., Zhang, R., 2018. Particle acidity and sulfate production during severe haze events in China cannot be reliably inferred by assuming a mixture of inorganic salts. Atmos. Chem. Phys. 18, 10123–10132.

Wang, H., Shi, G., Tian, M., Zhang, L., Chen, Y., Yang, F., Cao, X., 2017a. Aerosol optical properties and chemical composition apportionment in Sichuan Basin, China. Sci. Total Environ. 577, 245–257.

Wang, Q., Huang, R.J., Cao, J., Han, Y., Wang, G., Li, G., Wang, Y., Dai, W., Zhang, R., Zhou, Y., 2014. Mixing state of black carbon aerosol in a heavily polluted urban area of China: implications for light absorption enhancement. Aerosol Sci. Technol. 48, 689–697.

Wang, Q., Sun, Y., Jiang, Q., Du, W., Sun, C., Fu, P., Wang, Z., 2015. Chemical composition of aerosol particles and light extinction apportionment before and during the heating season in Beijing, China. J. Geophys. Res. Atmos. 120, 12708–12722.

Wang, Q., Huang, R.-J., Cao, J., Tie, X., Shen, Z., Zhao, S., Han, Y., Li, G., Li, Z., Ni, H., Zhou, Y., Wang, M., Chen, Y., Su, X., 2016. Contribution of regional transport to the black carbon aerosol during winter haze period in Beijing. Atmos. Environ. 132, 11–18.

Wang, Q., Cao, J., Han, Y., Tian, J., Zhang, Y., Pongpiachan, S., Zhang, Y., Li, L., Niu, X., Shen, Z., Zhao, Z., Tipmanee, D., Bunsomboonsakul, S., Chen, Y., Sun, J., 2018. Enhanced light absorption due to the mixing state of black carbon in fresh biomass burning emissions. Atmos. Environ. 180, 184–191.

Wang, T., Cheung, V.T.F., Anson, M., Li, Y.S., 2001. Ozone and related gaseous pollutants in the boundary layer of eastern China: overview of the recent measurements at a rural site. Geophys. Res. Lett. 28, 2373–2376.

Wang, X., Huang, J., Zhang, R., Chen, B., Bi, J., 2010. Surface measurements of aerosol properties over northwest China during ARM China 2008 deployment. J. Geophys. Res. Atmos. 115, D00K27.

Wang, Y., Zhang, Q.Q., He, K., Zhang, Q., Chai, L., 2013. Sulfate-nitrate-ammonium aerosols over China: response to 2000-2015 emission changes of sulfur dioxide, nitrogen oxides, and ammonia. Atmos. Chem. Phys. 13, 2635–2652.

Wang, Y.C., Huang, R.J., Ni, H.Y., Chen, Y., Wang, Q.Y., Li, G.H., Tie, X.X., Shen, Z.X., Huang, Y., Liu, S.X., Dong, W.M., Xue, P., Frohlich, R., Canonaco, F., Elser, M., Daellenbach, K.R., Bozzetti, C., Haddad, I.E., Prevot, A.S.H., Canagaratna, M.R., Worsnop, D.R., Cao, J.J., 2017b. Chemical composition, sources and secondary processes of aerosols in Baoji city of northwest China. Atmos. Environ. 158, 128–137.

Watson, J.G., 2002. Visibility: science and regulation. J. Air. Waste. Manage. 52, 628–713.

Wei, Y., Zhang, Q., Thompson, J.E., 2013. Atmospheric black carbon can exhibit enhanced light absorption at high relative humidity. Atmos. Chem. Phys. Discuss. 13, 29413–29445.

Xia, Y.J., Tao, J., Zhang, L.M., Zhang, R.J., Li, S.L., Wu, Y.F., Cao, J.J., Wang, X.J., Ma, Q.X., Xiong, Z., 2017. Impact of size distributions of major chemical components in fine particles on light extinction in urban Guangzhou. Sci. Total Environ. 587–588, 240–247.

Xu, H.M., Cao, J.J., Chow, J.C., Huang, R.J., Shen, Z.X., Chen, L.W.A., Ho, K.F., Watson, J.G., 2016a. Inter-annual variability of wintertime $PM_{2.5}$ chemical composition in Xi'an, China: evidences of changing source emissions. Sci. Total Environ. 545, 546–555.

Xu, X., Zhao, W., Zhang, Q., Wang, S., Fang, B., Chen, W., Venables, D.S., Wang, X., Pu, W., Wang, X., Gao, X., Zhang, W., 2016b. Optical properties of atmospheric fine particles near Beijing during the HOPE-J3A campaign. Atmos. Chem. Phys. 16, 6421–6439.

Yang, M., Howell, S.G., Zhuang, J., Huebert, B.J., 2009. Attribution of aerosol light absorption to black carbon, brown carbon, and dust in China – interpretations of atmospheric measurements during EAST-AIRE. Atmos. Chem. Phys. 9, 2035–2050.

Zhang, Q., Shen, Z.X., Cao, J.J., Zhang, R.J., Zhang, L.M., Huang, R.J., Zheng, C.J., Wang, L.Q., Liu, S.X., Xu, H.M., Zheng, C.L., Liu, P.P., 2015. Variations in $PM_{2.5}$, TSP, BC, and trace gases (NO_2, SO_2, and O_3) between haze and non-haze episodes in winter over Xi'an, China. Atmos. Environ. Times 112, 64–71.

Zhao, X.J., Zhao, P.S., Xu, J., Meng, W., Pu, W.W., Dong, F., He, D., Shi, Q.F., 2013. Analysis of a winter regional haze event and its formation mechanism in the North China Plain. Atmos. Chem. Phys. 13, 5685–5696.

Zhou, Y.Q., Wang, Q.Y., Huang, R.J., Liu, S.X., Tie, X.X., Su, X.L., Niu, X.Y., Zhao, Z.Z., Ni, H.Y., Wang, M., Zhang, Y.G., Cao, J.J., 2017. Optical properties of aerosols and implications for radiative effects in Beijing during the Asia-Pacific economic cooperation summit 2014. J. Geophys. Res. Atmos. 122, 10119–10132.

Zieger, P., Fierz-Schmidhauser, R., Weingartner, E., Baltensperger, U., 2013. Effects of relative humidity on aerosol light scattering: results from different European sites. Atmos. Chem. Phys. 13, 10609–10631.